RSC Advances

PAPER

View Article Online
View Journal | View Issue

Cite this: *RSC Adv.*, 2019, **9**, 38687

Fused pyrazole-phenanthridine based dyads: synthesis, photo-physical and theoretical studies, and live cell pH imaging†

Venkatesan Muthukumar,[a] Sathishkumar Munusamy,[b] Krishnan Thirumoorthy,[a] Sathish Sawminathan[a] and Sathiyanarayanan Kulathulyer*[a]

Received 27th September 2019
Accepted 7th November 2019

DOI: 10.1039/c9ra07860f

rsc.li/rsc-advances

The arrangement of small sized molecules with a scaffold structure plays an active role in the fields of sensors and health care. An efficient molecular design strategy for four pyrazole-phenanthridine based D–π–A luminophores, denoted as **2a**, **2b**, **2c** and **2d** was developed to investigate the effect of acid on the photo-physical properties of these dyes. Photo-physical studies of the synthesized probes showed distinct absorption and emission under various pH conditions. Theoretical calculations using density functional methods were carried out for understanding the mechanistic aspects of the proton induced fluorescence. The experimentally observed photo-physical properties correlated well with theoretical results. Moreover, probes **2** and **2a** can be used to monitor the fluorescence changes in *E. coli* cells under different pH conditions.

Introduction

Functional organic compounds, especially, stimuli-responsive organic emissive materials, have gained considerable attention in materials science,[1–8] medicine,[9–12] biology[13–16] and environmental analytics.[17–21] Among them, the acidochromic materials, whose emission response depends on the pH of the medium, have received considerable attention because they find applications in various fields of scientific research such as environment, ecology, agriculture, and biological processes. Facile and accurate measurement of pH is essential to study many chemical and physiological processes including the regulation mechanisms of cells. Among the various analytical methods, fluorescence pH sensors have many advantages such as high sensitivity and selectivity, rapid response, and low cost.[22,23] Most of the fluorescence probes for pH sensing, can sense in the "on–off (or off–on)"mode[24–28] and are less advantageous than "off–on–off" sensors. Unfortunately, the development of "off–on–off" sensors demands complex molecular design to meet the structural and electronic properties. Fluorescence probes to sense pH, based on various fluorophores such as xanthenes, BODIPY, cyanine, rhodamine, and phthalimide[29–34] have been developed. However, these sensors lack the key qualities such as photostability of the probe and reversibility.

Our ongoing research program is on the development of fluorescent probes for multifield applications.[35–37] Among the various probes that we developed, phenanthridine based materials are significant because of their tunable fluorescence nature. Recently, we have developed functionalized phenanthridine based probe for the selective detection Ru(III).[38] In the current work, we report the facile synthesis, characterization and studies on pH sensing ability of fused pyrazole-phenanthridine derivatives. The characterization of the synthesized molecules was carried out by different spectroscopic techniques and X-ray crystallography to confirm the structure of the probes. In the synthesized probe, both pyridine and pyrazole act as donor moiety, which results in weak fluorescence. The synthesized probe undergoes protonation over the addition of H^+ which results in the formation of pyridinium ion. The formation of pyridinium ion yielded D–π–A type dyes with intramolecular charge transfer (ICT) emission (Fig. 1) in which pyrazole acts as a donor and pyridinium ion acts as an

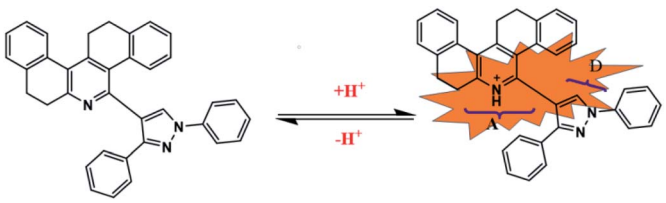

Fig. 1 Structure of the synthesized probe and design rational.

[a]*Chemistry Department, School of Advanced Sciences, Vellore Institute of Technology University, Vellore-632014, Tamil Nadu, India. E-mail: venket.chem88@gmail.com*
[b]*Institute of Physical Sciences, National Autonomous University of Mexico, Mexico*

† Electronic supplementary information (ESI) available. CCDC 1561810 and 1561812. For ESI and crystallographic data in CIF or other electronic format see DOI: 10.1039/c9ra07860f

acceptor. The induced color change is visible even to the naked eye. In addition, the greenish yellow fluorescence induced by trifluoroacetic acid can be reversed to its original fluorescence over the addition of triethylamine. More importantly, the synthesized probes have excellent selectivity towards H^+ over other metal ion and another competitive moiety. The synthesized probes have excellent cell permeability, and are applied successfully to monitor pH fluctuations in living cells. Computational studies are gaining great interest from the experimentalist view point to speculate various aspects in interpreting the experimental results. The use of Density Functional Theory (DFT) and Time-Dependent DFT (TDDFT) methods have been prominent in recent times for predicting the photo-physical properties and they are widely found in the literature.[39–41] In particular, the photo-physical studies of different compounds to understand the unexpected solvent effect and acidochromic fluorescence were reported elsewhere. In view of that, theoretical calculations were carried out for the molecules of our interest, such as probe **2a** and **2b** with implicit solvation model first. Further, one TFA molecule is explicitly considered to observe the intermolecular interaction with **2a** and **2b** separately, and is named as **2a-TFA** and **2b-TFA**, which would eventually shed light on the experimentally observed photo-physical properties.

Experimental section

Chemicals and apparatus

Starting material used for synthesis and solvents for the analytical use were bought from commercial sources and were used as such without any further purification. The molecular weight of the compound was obtained using JEOL GCMATE mass spectrometer. ^{1}H and ^{13}C NMR was obtained using Bruker Ascend III 400 MHz spectrometer using $CDCl_3$, UV spectra were recorded using Shimadzu 3600 spectrometer with a quartz cell (path length = 1 cm) at room temperature. Emission spectra were recorded using Hitachi High Technologies spectrometer. Single crystal X-ray diffraction was carried out with Bruker Kappa APEXII.

Procedure for the synthesis of probes and characterization

Compound **1** and its derivatives were synthesized according to the procedure stated in literature,[49] while compound **2** was prepared according to the following procedure. In an oven dried conical flask, ammonium acetate was (2 mmol) taken and dissolved in ethanol solvent. To this, compound **1** was added (2 mmol) and warmed. To this reaction mixture, two equivalents of 2-tetralone were added and the reaction mixture was stirred overnight. The completion of the reaction was monitored by TLC. Column chromatography was carried out for the reaction mixture over silica gel. Compound **2** was separated in 2% ethyl acetate in hexane. Yield: 65%. ^{1}H NMR and ^{13}C were recorded by dissolving compounds in $CDCl_3$ solvent. Chemical shifts (δ) are given in ppm relative to TMS internal standard.

1,3-Diphenyl-1*H*-pyrazole-4-yl-7,8,13,14-tetrahydrodibenzo[*a*,*i*]phenanthridine (2a). ^{1}H NMR (400 MHz, $CDCl_3$): δ 8.32 (s, 1H), 7.87–7.85 (d, J = 8 Hz, 2H), 7.72–7.68 (q, J = 16 Hz, 3H), 7.42–7.40 (d, J = 8 Hz, 1H), 7.34–7.33 (t, J = 4 Hz, 3H), 7.22–7.20 (d, J = 8 Hz, 1H), 7.17–7.16 (d, J = 4 Hz, 2H), 7.10–7.06 (d, J = 16 Hz, 3H), 7.06–6.99 (m, 1H), 7.00–6.99 (d, J = 4 Hz, 1H), 6.97–6.91 (m, 2H), 3.17–3.14 (t, J = 12 Hz, 3H), 3.07–3.04 (t, J = 12 Hz, 4H), 2.41–2.37 (p, J = 20 Hz, 2H). ^{13}CNMR (400 MHz, $CDCl_3$): δ 158.3, 158.6, 151.6, 145.9, 145.5, 140.0, 139.5, 138.5, 136.8, 133.0, 132.9, 129.7, 129.0, 128.7, 128.3, 128.0, 127.9, 127.7, 127.5, 127.3, 127.2, 127.1, 127.0, 126.85, 126.5, 126.4, 126.3, 126.1, 125.8, 123.1, 121.2, 118.9, 112.9, 33.1, 31.3, 30.9, 29.5, 29.0, 28.7. The obtained mass value for compound **2a** is 502.2202 m/z (ESI Fig. 17†).

5-(1-(4-Methoxyphenyl)-3-phenyl-1*H*-pyrazole-4-yl)-7,8,13,14-tetrahydrodibenzo[*a*,*i*]phenanthridine (2b). ^{1}H NMR (400 MHz, $CDCl_3$): δ 8.23 (s, 1H), 7.81–7.79 (d, J = 8 Hz, 2H), 7.49–7.45 (q, J = 16 Hz, 4H), 7.37–7.35 (d, J = 8 Hz, 1H), 7.31–7.27 (p, J = 20 Hz, 3H), 7.18–7.16 (d, J = 8 Hz, 1H), 7.09–7.07 (d, J = 8 Hz, 2H), 7.00–6.96 (q, J = 16 Hz, 1H), 6.93–6.88 (m, 2H), 6.59–6.57 (d, J = 8 Hz, 2H), 6.94–6.91 (t, J = 12 Hz, 2H), 3.69 (s, 3H), 3.11–3.08 (q, J = 16 Hz, 3H), 3.02–3.01 (d, J = 4 Hz, 3H), 2.41–2.38 (q, J = 16 Hz, 2H), 2.16 (s, 6H); ^{13}CNMR (400 MHz, $CDCl_3$): δ 206.9, 159.0, 158.3, 146.1, 145.4, 140.0, 139.5, 138.5, 133.0, 132.9, 129.3, 128.7, 128.4, 127.9, 127.76, 127.72, 127.30, 127.05, 126.47, 126.20, 126.12, 125.89, 125.87, 123.51, 118.89, 113.47, 113.19, 77.42, 77.30, 77.10, 76.78, 55.27, 33.20, 30.94, 29.53, 29.16, 29.0. The obtained mass value for compound **2a** is 502.2202 m/z (ESI Fig. 18†).

5-(1-(4-Bromophenyl)-3-phenyl-1*H*-pyrazole-4-yl)-7,8,13,14-tetrahydrodibenzo[*a*,*i*]phenanthridine (2c). ^{1}H NMR (400 MHz, $CDCl_3$): δ 8.27 (s, 1H), 7.81–7.79 (d, J = 8 Hz, 2H), 7.48–7.44 (q, J = 12 Hz, 4H), 7.38–7.35 (t, J = 12 Hz, 1H), 7.30–7.28 (d, J = 8 Hz, 3H), 7.16–7.11 (m, 3H), 7.01–6.99 (t, J = 12 Hz, 3H), 6.96–6.94 (d, J = 8 Hz, 5H), 3.11–3.01 (m, 6H), 2.41–2.39 (t, J = 12 Hz, 2H). ^{13}C NMR (400 MHz, $CDCl_3$): δ 158.5, 150.3, 145.56, 145.5, 139.9, 139.5, 132.9, 132.0, 130.6, 129.4, 128.8, 127.9, 127.8, 127.3, 127.2, 126.5, 126.1, 125.9, 123.8, 121.4, 119.0, 33.1, 30.9, 29.5, 29.0.

5-(1-(4-Methoxyphenyl)-3-phenyl-1*H*-pyrazole-4-yl)-7,8,13,14-tetrahydrodibenzo[*a*,*i*]phenanthridine (2d). ^{1}H NMR (400 MHz, $CDCl_3$): δ 9.24 (s, 1H), 8.88–8.86 (d, J = 8 Hz, 1H), 8.21–8.19 (d, J = 8 Hz, 1H), 8.06–8.00 (m, 3H), 7.87–7.85 (d, J = 8 Hz, 1H), 7.80 (s, 1H), 7.77 (s, 1H), 7.75 (s, 1H), 7.73–7.71 (d, J = 8H, 1H), 7.69 (s, 1H), 6.64–6.61 (t, J = 12 Hz, 1H), 7.58–7.57 (d, J = 4 Hz, 1H), 7.53 (s, 1H), 7.49 (s, 1H), 7.36–7.31 (m, 1H), 2.17 (s, 3H), 1.25 (s, 3H). ^{13}C NMR (400 MHz, $CDCl_3$): δ 135.7, 133.6, 131.2, 129.5, 129.1, 128.9, 128.6, 126.9, 126.8, 123.3, 126.1, 125.7, 125.2, 125.0, 123.4, 123.2, 121.3, 121.1, 121.0, 120.1, 119.5, 116.7, 112.8, 105.5, 30.9, 29.7, 29.3, 14.15.

Computational calculation methods

Computational chemistry calculations were carried out to understand the experimentally observed photo-physical properties in TFA solvent polarity. The reported molecules in the present work such as **2a**, **2b**, **2a-TFA** and **2b-TFA** were first optimized in gas phase and later in solution phase by considering the dielectric medium of the TFA solvent. The structural optimization of **2a**, **2b**, **2a-TFA** and **2b-TFA**

molecules was carried out using DFT methods. In DFT, the well-known exchange–correlation functional (XC) function, Becke 3-parameter (B3) combined with Lee–Yang–Parr (LYP)[42,43] correlation functional, popularly called as B3LYP was utilized in the present work. The B3LYP functional with 6-31+G* split valence basis set was used for all the computational calculations. The integral equation formalism (IEF) version of the polarizable continuum model (PCM)[44] was employed to incorporate the solvent effects in the computational calculations. The ground state optimized geometries obtained in gas phase and also in TFA solvent phase were used separately to find the singlet excited state structure of **2a**, **2b**, **2a-TFA** and **2b-TFA** molecules with TDDFT[45,46] method. All TD-DFT calculations were carried out using single point calculation from optimized geometries of **2a**, **2b**, **2a-TFA** and **2b-TFA** at B3LYP/6-31+G* level of theory. The positive frequencies obtained from the normal mode analysis for all ground state geometries ascertained that all the optimized structures were in their global minimum. All the quantum chemical calculations were performed with Gaussian 09W package.[47] The structures and electron density plots were obtained with help of GaussView 5.0 program.[48]

Cell toxicity assay evaluation

The cytotoxicity of compound **2a** and **2b** against *E. coli* bacteria was estimated using liquid Luria–Bertani medium (LB). From this 400 μL of freshly prepared *E. coli* culture (10 h) was centrifuged at 3000 rpm for 20 min at 4 °C. Supernatant liquid Luria–Bertani medium (LB) was removed, and the pellet containing bacterial cells was washed twice with 800 μL PBS (150 mM NaCl, pH 7.4) followed by centrifugation at 3000 rpm for 20 min at 4 °C. The pellet with bacterial cells alone is used as control. The final pellet containing purified bacterial cells were mixed with 50 μL PBS containing probe **2a** (in 1 : 1 v/v THF–water). In this absorbance was monitored by microplate reader. The cell viability was expressed by the difference in absorbance of samples and control. This same procedure was repeated for the compound **2b** also. The percentage of cell growth inhibition was calculated by the following formula % cytotoxicity = 100 − % cell viability.

Results and discussion

Design and synthesis

The synthesis of (1,3-diphenyl-1*H*-pyrazole-4-yl)-7,8,13,14-tetrahydrodibenzo[*a*,*i*]phenanthridine is outlined in Scheme 1. Precursor **1a** and its derivatives**1b–d** were prepared by following the literature procedure. Probes **2a–d**, the subject material, were facilely synthesized by the reaction of the respective aldehydes **1a–d** with β-tetralone and ammonium acetate following a method that was previously reported by our research group. All the synthesized compounds were thoroughly characterized by ^{1}H NMR, ^{13}C NMRand mass spectroscopy. Compound **2** and **2a** was recrystallized by a slow evaporation method using ethanol–THF mixture and the

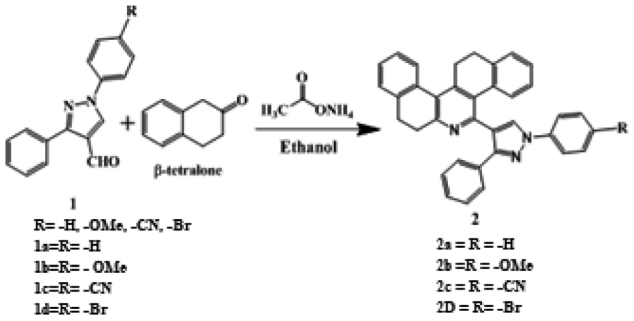

Scheme 1 Synthesis of probe **2**.

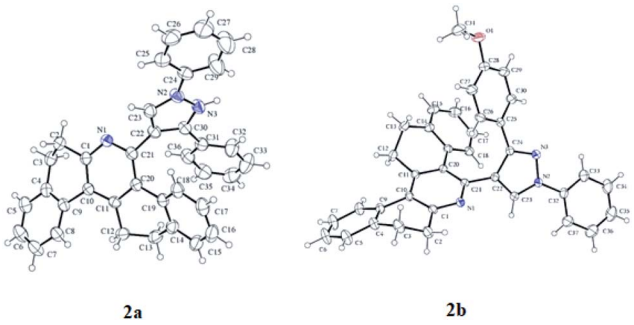

Fig. 2 Crystal structure of compound **2a** and **2b**.

crystal structure of the compound was elucidated using the X-ray diffraction technique (Fig. 2).

Probes **2a–d** was designed to have a phenanthridine fluorophore capable of interacting with H^+ and pyrazole, which was an electron donor that weakened the emission of phenanthridine. It was designed in a manner that when the probe interacted with H^+, the subsequent formation of pyridinium ion induced D–π–A type of ICT system and the fluorescence of the probe would be switched on. The pyridinium ion state of the probe can be brought back to pyridine state by introducing triethylamine (TEA) and the fluorescence can be turned off.

Influence of H^+ on the absorption and emission properties of the probes

The optical property of the acid sensitive molecule can be perturbed by the change in electronic delocalization in a molecule over the addition of protons. Generally, the nitrogen hetero atom containing fluorophores is responsible for acidochromism because of the availability of the lone pair of electrons on the nitrogen to bind with protons. In order to study the acidochromic property of the synthesized molecules, we analysed the proton-sensing ability of the compounds **2a–2d**, which arise from the proton binding property of pyridine moiety. The normalized UV-vis absorption of compounds **2a** to **2d** is shown in Fig. S19† and their related photo-physical parameters are given in Tables 1 and 2. Distinct effects of substituent on their electronic properties, such as, large Stokes shift (1: 151 nm; 2: 130 nm; 3: 176 nm) and high molar absorptions were observed. Compound **2a** and **2b** exhibited similar absorption spectra with

Table 1 Photo-physical parameters of compound **2a**, **2b**, **2c** and **2d** before the addition of TFA

	λ_{abs} (nm)	$\varepsilon_{max} \times 10^4$ (M^{-1} cm^{-1})	λ_{em}[a] (nm)	SS[b]	Φ_f[c]
2a	267, 320	2.70, 1.00	392, 414, 446	125	0.20
2b	267, 320	2.75, 1.07	397	130	0.17
2c	271, 367	2.15, 0.25	369, 386, 405	98	0.23
2d	271, 367	2.05, 0.41	368, 386, 407	97	0.15

[a] Emission wavelength. [b] Stocks shift. [c] Quantum yield.

Table 2 Photo-physical parameters of compound **2a**, **2b**, **2c** and **2d** after the addition of TFA

	λ_{abs} (**2** + TFA) (nm)	λ_{em} (**2** + TFA) (nm)	SS (**2**+ TFA) (nm)	Φ_f (**2** + TFA)
2a	279, 315	463	196	0.11
2b	265, 318	457	190	0.07
2c	270, 367	—	—	—
2d	—	—	—	—

two distinct absorption maxima. The peak at 269 nm was due to the n–π* transition and the peak at 320 is attributed to the π–π* transition. However, in compound **2c** and **2d**, the absorption peak responsible for n–π* transition had slight bathochromic shift and appeared at 270 nm and 272 nm respectively. Furthermore, the π–π* transition had phenomenal redshift and appeared in the region of 367 nm. This can be explained on the basis of their extended conjugation and development of ICT due to the presence of electron donating (–Br) and withdrawing (–CN) groups.

We initially evaluated the changes in the UV-visible spectrum of probes with and without the addition of H^+. In this study, trifluoroacetic acid (TFA) was chosen as the acid source. Probe **2a** was dissolved in chloroform solvent and the absorption spectra were recorded. To this solution, when TFA was added, the intensity of the peak at 267 nm progressively decreased with bathochromic shift and the peak at 320 nm completely disappeared (Fig. 3). In addition, a new peak originated at the excitation wavelength of 367 nm. This clearly indicated that intramolecular charge transfer was induced over the addition of TFA. Considering the new absorption at *ca.* 367 nm, TFA-protonated **2a** in $CHCl_3$ formed the cation **2a-H$^+$**. As shown in Fig. 3C, the ratio of absorption at 267 nm to that at 367 nm, A_{269}/A_{367} had good linear relationship with the increasing concentration of TFA for up to 10 equivalents. Furthermore, these absorption changes can be significantly reversed on neutralization with bases such as triethylamine (TEA). Almost similar absorption spectral changes were observed for **2b** upon the addition of TFA and TEA. Unfortunately, the absorption of the probes **2c** and **2d** was not affected by the TFA. Hence, further studies were carried out using only probes **2a** and **2b**.

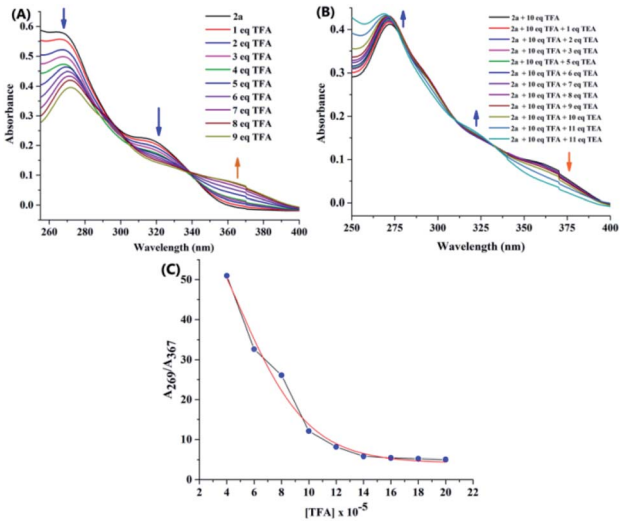

Fig. 3 (A) The absorption spectra of the compound **2a** (2×10^{-5}) in chloroform solvent over the addition of TFA. (B) The absorption spectra of the compound **2b** with TFA over the addition of TEA. (C) The plot of abortion intensity ratio (A_{269}/A_{367}) *vs.* the concentration of TFA.

Fig. S21† shows the normalized emission spectra of the probes **2a** and **2b** at concentration 5×10^{-5} M in chloroform solvent. When excited at 269 nm, probe **2a** exhibited three intense peaks at 392 nm, 414 nm and a shoulder peak at 446 nm, whereas, probe **2b** displayed an intense emission at

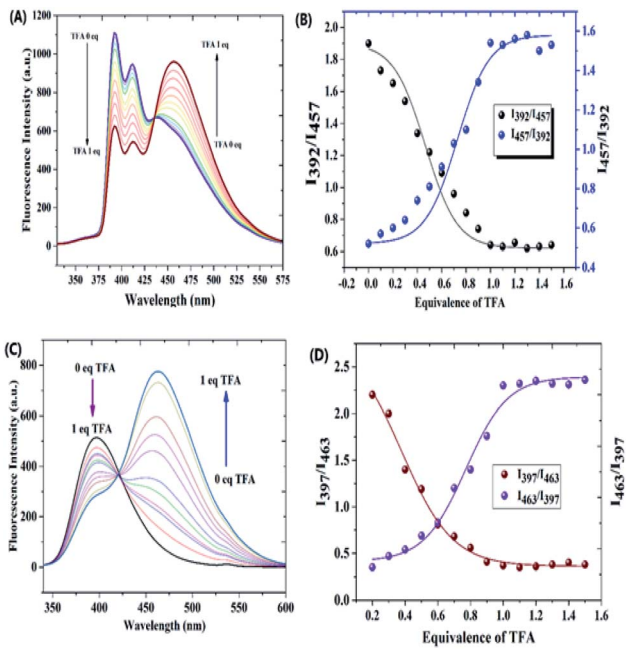

Fig. 4 (A) Emission spectra of the compound **2a** (2×10^{-5}) in chloroform solvent over the addition of TFA ($\lambda_{ex} = 267$ nm). (B) Sigmoidal fitting of fluorescence intensity ration I_{392}/I_{457} *vs.* equivalence of TFA for compound **2a**. (C) Emission spectra of the compound **2b** (2×10^{-5}) in chloroform solvent over the addition of TFA ($\lambda_{ex} = 267$ nm). (D) Sigmoidal fitting of fluorescence intensity ration I_{397}/I_{463} *vs.* equivalence of TFA for compound **2a**.

397 nm. The extended conjugation in the pyrazole ring due to the presence of the methoxy group could be the reason behind the red-shifted emission maxima. The emission spectra of the compound **2a** and **2b** underwent significant ratiometric changes over the addition of TFA. The corresponding spectra are shown in Fig. 4A and C. In the case of probe **2a**, fluorescence intensities at 392 nm and 414 nm decreased progressively but it was accompanied by a remarkable increase in the redshifted fluorescence intensity at 457 nm (Fig. 4B). In probe **2b**, the intensity of the peak at 397 nm decreased progressively with a concomitant increase in the intensity of the redshifted peak at 463 nm (Fig. 4D). A well-defined iso emissive point in the emission spectra suggested that the only reaction was the binding of ligand with the proton. We think that the emergence of new emission peak at the higher wavelength is due to the formation of ICT which arises due to the protonation of the probes (Fig. 5). Furthermore, the shift of two emission wavelengths are large ($\Delta F = 65$ nm for **2a**; $\Delta F = 66$ nm for **2b**) which contributes to the accurate measurement of emission intensities. As shown in the Table 1, addition of TFA to the probe **2a** increased the stokes shift from 125 nm to 196 nm for probe **2a** and from 130 nm to 190 nm for probe **2b**. It was noted that the fluorescence quantum yields (Φ_f) for the probes **2a** and **2b** decreased significantly for the protonated form (Table 1). The linear ratiometric fluorescence response of the probes towards TFA concentration is of particular importance. The ratio of the emission intensity I_{392}/I_{457} for **2a** and I_{397}/I_{463} for **2b** has linear correlation with the concentration of TFA. The linear equation was found to be $y = 0.0000096 + 0.4$ for **2a** and $y = 0.000023 + (-0.33)$ for **2b** (Fig. S22†) indicating that probes **2a** & **2b** can quantitatively detect H^+ concentration. Furthermore, clear fluorescence color change was observed for compound **2a** from blue to green while adding TFA as shown in the Fig. 5.

Reversibility of the receptor

The possible deprotonation of the probe **2a** and **2b** and its fluorescence spectrum over the addition of TEA was monitored. On addition of TEA, the fluoresce spectrum of protonated species **2a-H$^+$** and **2b-H$^+$** got completely reversed and fluoresce

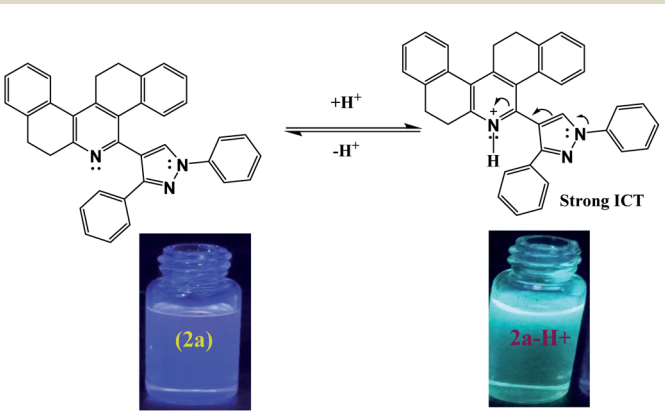

Fig. 5 Mechanism of protonation of compound **2a** and the fluorescence color change of the probe over acidification.

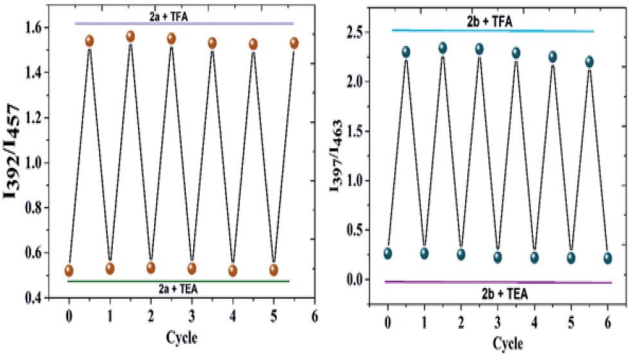

Fig. 6 The fluorescence intensity ration of **2a** and **2b** upon consecutive addition of TFA and TEA for up to six cycles.

spectrum almost similar to that of free **2a** and **2b** was obtained (Fig. S23†). The reversible behaviour of the probe **2a** and **2b** is shown in Fig. 6. The fluorescence of the protonation and deprotonation states for both the probes was reversed for up to six cycles without much variation in the intensity of fluorescence. Hence, this probe can be used multiple times to analyse the proton concentration.

Emission properties of the probes towards pH

The fluorescence spectroscopic property of the probes was studied in different pH buffers containing 50% ACN. Probe **2a** exhibited fluorescence emission at 392 nm, and when pH of the buffer was higher than 7.0 no new emission bands were observed. As shown in the Fig. 7, when the pH of the medium was decreased from 7 to 1, gradual emergence of new emission peak was observed at 457 nm. In addition, the fluorescence emission of the compounds changed from blue to yellowish green under UV light irradiation (Fig. 7C) suggesting the potential of the probe **2a** to sense the different pH conditions of

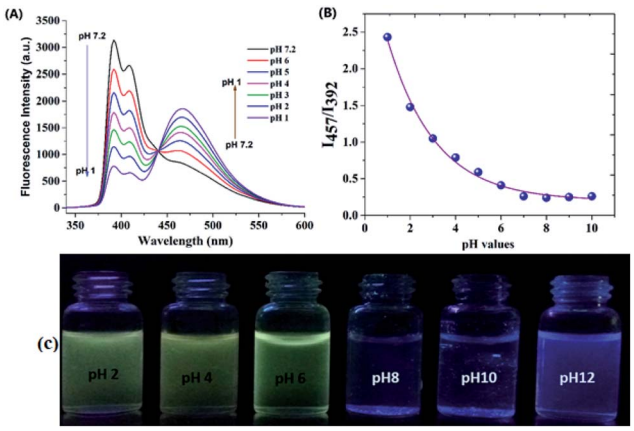

Fig. 7 (A) The fluorescence spectra of compound **2a** ($\lambda_{ex} = 267$ nm, 2×10^{-4} M) in acetonitrile: buffer mixture at different pH. (B) Boltzmann fitting curve of fluorescence intensity ratio (I_{457}/I_{392}) *vs.* different pH values in buffer solutions. (C) Fluorescence color change of **2a** under various pH solution.

the medium. The pK_a was calculated at abrupt points by plotting Boltzmann fitting curve as shown in the Fig. 7B. The pK_a was found to be 3.12 ± 0.02 indicating the excellent pH sensing ability of probe **2a**.

Even though probe **2b** showed significant fluorescence ratiometric behaviour with TFA in chloroform, its effect on pH was relatively less. This could due to the water intolerance of the probe **2b**.

The optical properties in different solvents

We try to optimize the quantum efficiency of compound **2a** and **2b** in different types of solvents. This showed that distinct interaction of the molecules in non-polar and polar solvents. While increasing the solvent polarity, the spectrum showed red shift with lower intensity. It may be due to the dipole interaction between lone pair of pyridine nitrogen and H^+ ion from polar solvent (Fig. 8) and Table 3.

Selectivity and anti-interference studies

The selectivity and anti-interference of this probe to H^+ was examined by measuring the fluorescence spectra of the probes

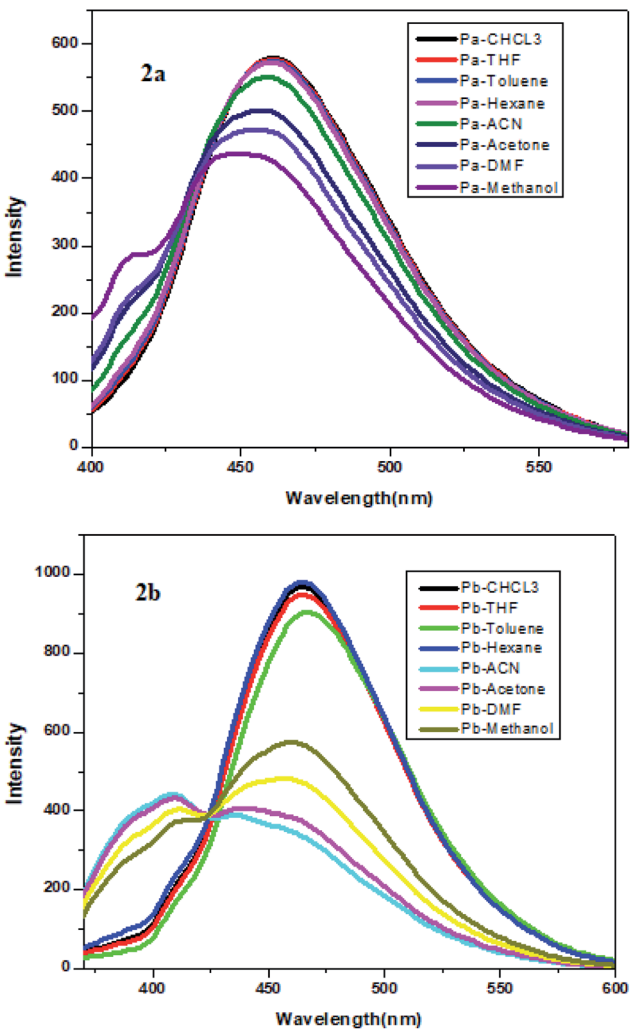

Fig. 8 The solvent effect of **2a** and **2b**.

Table 3 The quantum yield of **2a** and **2b** in different solvent

	Pa		Pb	
	λ_{em} (nm)	$\Phi_f{}^a$	λ_{em} (nm)	$\Phi_f{}^a$
Low polar solvent				
$CHCl_3$	461.22	0.20	464.84	0.17
THF	461.22	0.18	464.84	0.17
Toluene	460.78	0.19	467.70	0.18
Hexane	460.71	0.18	464.84	0.18
High polar solvent				
Acetonitrile	459.42	0.20	408, 437	0.17
Acetone	456.26	0.18	409, 440	0.17
Dimethelyformate	455.82	0.19	399, 459	0.18
Methanol	413, 449	0.18	409, 461	0.18

[a] Fluorescence quantum yield.

with competing ions, such as, metal ions (Pb^{2+}, Ni^{2+}, Fe^{2+}, Cu^+, Zn^{2+}, Cd^+, Ag^{2+}, Pd^{2+}, Hg^{2+}, Cu^{2+}, Cr^{3+}, Fe^{3+}, Al^{3+}, Hg^{2+}), anions (F^-, Cl^-, I^-, HCO_3^-, CH_3COO^-) and thiol involved biomolecules (cysteine). As shown in Fig. 9, other ions and small molecules induced no obvious change or quenching effect on the fluorescence spectra of the probe **2a**. Similar selectivity of H^+ was observed for compound **2b** also (Fig. S24†). The fluorescence sensing study of the probe towards H^+ was also studied in the presence the ions mentioned above. The results demonstrated that the presence of other ion had no influence on the detection H^+. These results suggest that the probes have good selectivity and anti-interference ability towards the detection of H^+.

Theoretical results

Theoretical calculations were performed using DFT and TDDFT methods in phases, the gas phase and the solution phase, for understanding the structural properties of the investigated systems. The optimized geometry of probe **2a** is shown in

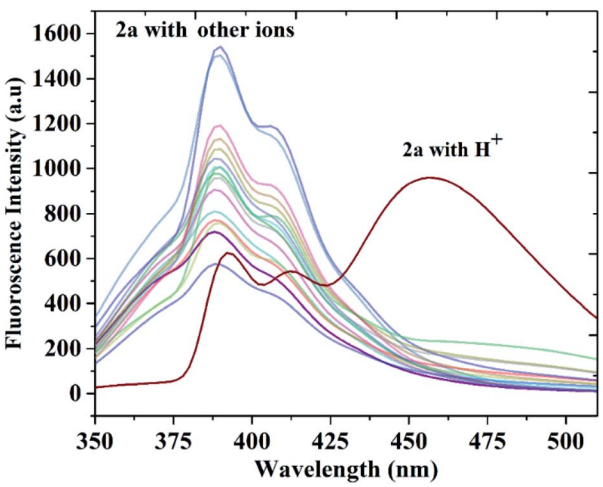

Fig. 9 The fluorescence spectra of probe **2a** (2×10^{-5} M) over the addition of various testing ion (10.0 equiv. for each ion) in 1 : 1 PBS buffer (pH = 7.4) and acetonitrile solvent. The $\lambda_{ex}$was set to be 267 nm.

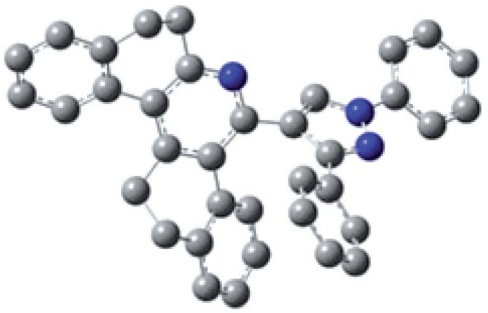

(2a)

Fig. 10 The optimized geometry of **2a** at B3LYP/6-31+G* level of theory. The implicit solvation model is used for structure optimization in TFA solvent. All hydrogen atoms are omitted for clarity.

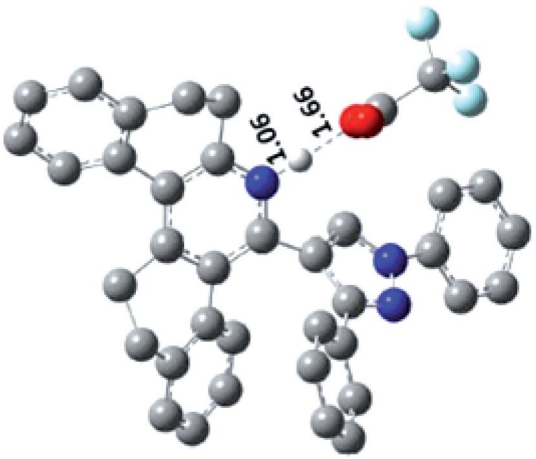

2A-TFA

Fig. 11 The optimized geometries of **2a** with TFA solvent, named as **2a-TFA**. The proposed solvent interaction is studied explicitly by considering one TFA molecule. In addition to that, the implicit solvation model is used for structure optimization in TFA solvent at B3LYP/6-31+G* level of theory. All hydrogen atoms are omitted for clarity.

Fig. 10. The energy minimized structure of probe **2b** is shown in Fig. S25.† Table 2 pre-sets the optimized geometrical parameters of probe **2a** at B3LYP/6-31+G* level of theory by comparing them with the available crystal structure. The selected structural parameters as shown in Table 4 are in good agreement with crystal geometry. The calculated bond length of N2–N3 was ~1.356 Å and bond angle N2–C23–C22 was ~107.6° for probe **2a**. Notable deviations in the calculated structural parameter were not observed at B3LYP/6-31+G* level of theory. Further, probes **2a** and **2b** were explicitly treated with one TFA (considered as **2a-TFA** and **2b-TFA** respectively) and **2a-TFA** and **2b-TFA** which were optimized with implicit solvation model. The optimized electronic structures of **2a-TFA** and **2b-TFA** are shown in Fig. 10 and S26† respectively (Fig. 11).

Table 4 The selected structural parameters of **2a** at B3LYP/6-31+G* level of theory and corresponding crystal data. The numbering scheme is followed as given for the probe **2a** in Fig. 2

	2a	
	B3LYP/6-31+G*	Crystal
Structural parameters	Bond length (Å)	
C1–N1	1.333	1.334
C24–N2	1.422	1.422
C23–N2	1.363	1.352
C30–N3	1.338	1.324
C21–N1	1.349	1.349
C30–C31	1.477	1.471
C21–C22	1.484	1.473
N2–N3	1.357	1.356
C18–C19	1.406	1.396
	2a	
	B3LYP/6-31+G*	Crystal
Structural parameters	Bond angle (°)	
N1–C1–C2	117.3	124.1
C1–C2–C3	109.8	110.5
N2–C23–C22	107.6	108
C29–C24–N2	119.7	119.7
C25–C24–N2	120	120.6
C36–C31–C30	121	121.4
N1–C21–C20	122	122.4

The TDDFT calculations were carried out for accounting excitation energy in TFA solvent using B3LYP/6-31+G* level of theory. The calculated UV-vis absorption wavelength of FMO pairs responsible for the excitation energy and its contribution in percentage is provided in Table 5. Compound **2a** showed itself as having electron rich pyrazole moiety, exhibiting excitation energy 326.3 nm, whereas **2a+H$^+$**, the acceptor pyridinium ion exhibited excitation energy 367.23 nm due to elongated conjugation with HUMO–LUMO transition. Similarly, the observed excitation energy difference between **2b** and **2b+H$^+$** was 59.53 nm with same HUMO–LUMO transition.

The Frontier Molecular Orbital's (FMO) density plots of probe **2a** and **2a-TFA** are shown in Fig. 12. Fig. S27† shows the FMO density plots of probe **2b** and **2b-TFA**. In the highest molecular orbital (HOMO), the electron density was mainly accumulated on pyrazole coordinated pyridine ring but in the lowest unoccupied molecular orbital (LUMO), it was localized on phenanthridine moiety. The calculated UV-vis spectra of **2a**, **2b**, **2a-TFA** and **2b-TFA** in TFA medium are shown in Fig. 13.

To understand the photo-physical properties of investigated systems, the absorption bands **2a** and **2a + H$^+$**were observed in gas phase and also in the acidic medium (TFA). The experimental results of the probe **2a** showed two peaks at 267 nm and 320 nm. The absorption intensity got enhanced to 279 nm and 315 nm when it was treated with solvent TFA. The theoretically calculated UV-vis wavelength absorption maximum, λ_{max} (nm) which was obtained by employing the TDDFT method in gas phase and also in TFA medium are provided in Table 6. The MO

Table 5 Calculated UV-vis absorption wavelength of FMO pairs responsible for the excitation energy and its contribution in percentage. All single point TDDFT calculations employed in optimized structures in TFA solvent medium

	PCM/B3LYP/6-31+G* in TFA solvent		
Structures	Excitation energy (nm)	FMO transition	FMO pair contribution (%)
2a	326.13	HOMO → LUMO	69
2b	336.44	HOMO → LUMO	70
2a-TFA	367.23	HOMO → LUMO	70
2b-TFA	395.97	HOMO → LUMO	70

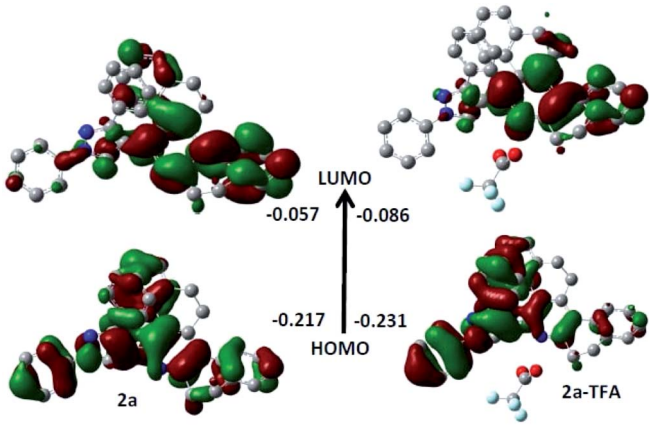

Fig. 12 FMO pairs responsible for the excitation energy in **2a** and **2a-TFA**. All orbitals are obtained from PCM/B3LYP/6-31+G* single point calculation in TFA solvent. Isovalue for surface = 0.02. All hydrogen atoms are omitted for clarity.

transition, which was responsible for λ_{max} in **2a** and **2a-TFA**, is shown in Fig. 14.

In **2a**, MO transition occurred from HOMO−2 to LUMO but in the case of **2a-TFA**, the MO transition happened from HOMO−2 to LUMO+1. Fig. S28† shows MO transitions which are responsible for the corresponding λ_{max} values in **2b** and **2b-TFA**. This happens because of HOMO to LUMO+2 in both cases. The computed results on MO transitions showed the single

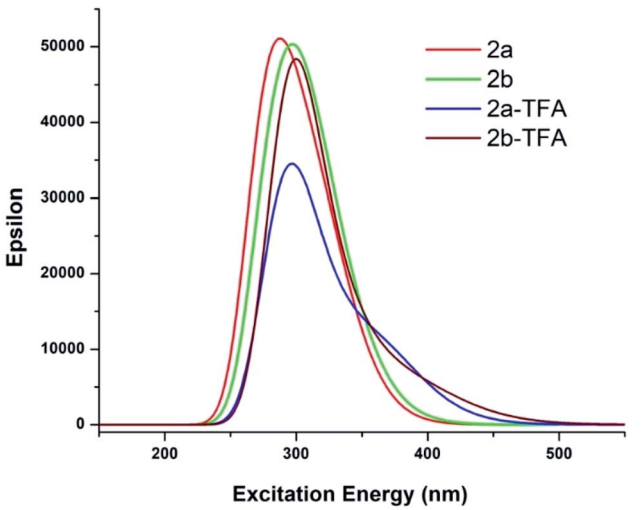

Fig. 13 UV-vis spectra of investigated molecules in TFA medium. All single point TDDFT calculations employed in optimized structures in TFA solvent medium at PCM/B3LYP/6-31+G* level of theory.

Table 6 Calculated UV-vis absorption wavelength of FMO pairs responsible for the excitation energy and its contribution in percentage. All single point TDDFT calculations employed in optimized structures in TFA solvent medium

		B3LYP/6-31+G* λ_{max} (nm)		Exp.
Structures	MO transition	Gas phase	TFA	λ_{max} (nm)
2a	HOMO−2 → LUMO	301	285	267, 320
2a-TFA	HOMO → LUMO+1	289	294	279, 315
2b	HOMO → LUMO+2	306	305	267, 320
2b-TFA	HOMO → LUMO+2	298	296	265, 318

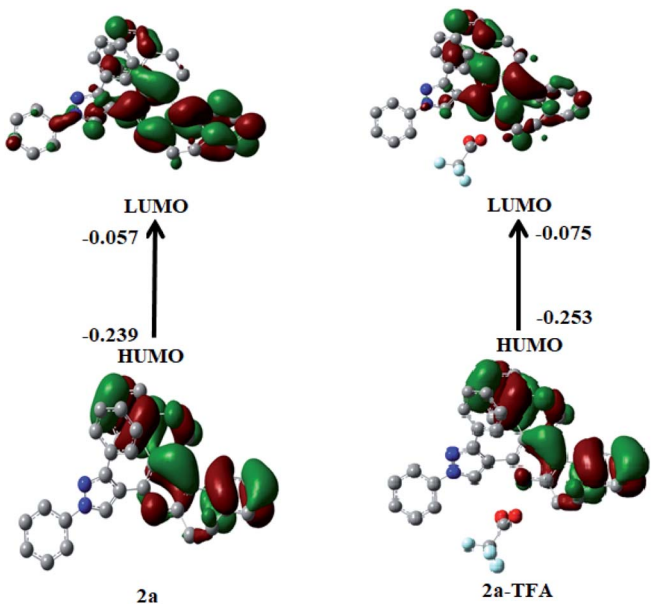

Fig. 14 The MO pairs responsible for UV-vis wavelength absorption maximum, λ_{max} (nm) in **2a** and **2a-TFA**. All orbitals are obtained from PCM/B3LYP/6-31+G* single point calculation in TFA solvent. Isovalue for surface = 0.02. All hydrogen atoms are omitted for clarity.

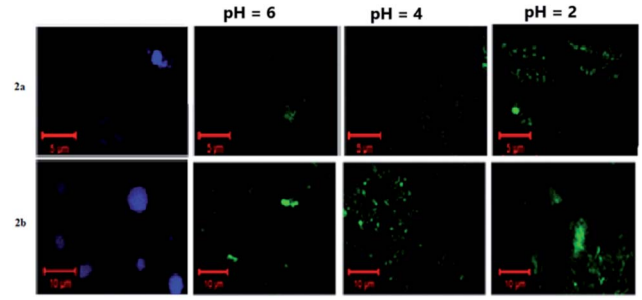

Fig. 15 Fluorescence microscopic images of living *E. coli* cells incubated with probe **2a** and **2b** for 30 min at 37 °C and then incubated with various pH buffers.

mode of peak at 285 nm in acidic medium and at 301 nm in gas phase and the MO transition was associated with HOMO−2 to LUMO for the probe **2a**. In TFA, with an explicit treatment with probe **2a**, the absorption band increased to 294 nm with HOMO−2 to LUMO+1 transition. This indicates that the electron density of pyrazole influenced by internal charge transfer in acidic medium, led to the formation of a rigid structure of donor–π–acceptor conjugation with pyridinium ion. Similarly, the absorption band of probe **2b** and **2b** + H^+ showed a single mode of peak at 306 nm in gas phase and 305 nm in solution phase by dominated HOMO–LUMO+2 transition. The observed absorption band slightly decreased from 298 nm in gas phase to 296 nm in TFA, thus accounting for the rigidity that occurred in the attachment of methoxy segment. As discussed above, theoretically computed photo-physical properties corroborated well with experimental data.

Application in living cell pH imaging

To demonstrate the pH sensing ability of the probes inside the cells, *Escherichia coli* (*E. coli*) cells were employed for cell imaging[50–52] at different pH values. An ionophore nigericin was used in order to allow the H^+ ions to pass through the cells to maintain the required pH in the cell. *E. coli* cells were treated with probes in PBS buffer (pH = 7.4) for 30 minutes at 37 °C and then washed three times with buffer solution of varying pH levels. The fluorescence microscope images of *E. coli* cells with probes **2a** and **2b** are shown in Fig. 15. *E. coli* cells exhibited bright blue color image when intracellular pH was 7.4, indicating that probes **2a** and **2b** were permeable to the cell membrane, and they successfully internalized into the cells. As shown in the Fig. 15, the bright blue emission of the cell completely vanished when the pH of the solution was altered from basic to acidic and bright green color was noticed. This cell imaging experiment was in good agreement with the results obtained in the aqueous solution, thus indicating the excellent bioimaging performance of the synthesized probes to detect the change of pH values in living cells.

Moreover, the cell viability (after incubation) with the *E. coli* bacteria at different concentration was estimated. The observed data indicates that cell viability remained above 85% upon incubation. This shows the cytotoxicity was present in negligible amount for compound **2a** and **2b**. The observed data were showed in Fig. S29.†

Conclusion

We have synthesized new class of fused phenanthridine-pyrazole compounds whose proton sensing ability originates from the induced intra molecular charge transfer mechanism. Probes **2a** and **2b** showed excellent fluorescent ratiometric behaviour over the addition of TFA. Moreover, the fluorescence property of the protonated probe can be reversed several times. The fluorescence of compound **2a** exhibited excellent pH-responsive abilities in the pH range of 7 to 1 with the pK_a value at 3.12. Further, probes **2a** and **2b** showed exceptional selectivity towards H^+ ion and the fluorescence was much less perturbed with other competitive ions and molecules. The acid responsive mechanism of the probes **2a** and **2b** was investigated by DFT and TDDFT methods. The experimentally observed photo-physical properties were well correlated with FMO transitions and their ponding excitation energy. The experiment of living cell imaging of pH showed remarkable bio-imaging performance of probes **2a** and **2b**.

Conflicts of interest

There is no conflict of interest.

Acknowledgements

The authors thank VIT Management for funding through seed money (Grand 2018-2019) and DST-FIST and VIT-SIF for FT-NMR facility and authors would like to thank Dr R. Srinivasan, SSL, Vellore Institute of Technology for language editing.

Notes and references

1 H. Ju, W. Kang, J. Zhang, H. Geng, Z. Liu, G. Zhang, Y. Zhao and D.-Q. Zhang, *Chem. Mater.*, 2017, **29**, 3580–3588.
2 A. Al Mousawi, F. Dumur, P. Garra, J. Toufaily, T. Hamieh, B. Graff, D. Gigmes, J. P. Fouassier and J. Lalevée, *Macromolecules*, 2017, **50**, 2747–2758.
3 A. Al Mousawi, P. Gaara, X. Sallenave, F. Dumur, J. Toufaily, T. Hamieh, B. Graff, D. Grimes, J. P. Fouassier and J. Lalevée, *Macromolecules*, 2017, **50**, 4913–4926.
4 H.-Y. Chen, G. Schweicher, M. Planells, S. Ryno, K. Broch, A. White, D. Simatos, M. Little, C. Jellett, S. Cryer, A. Marks, M. Hurhangee, J.-L. Bredas, H. Sirringhaus and I. McCulloch, *Chem. Mater.*, 2018, **30**, 7587–7592.
5 V. Prakasam, F. Di Giacomo, R. Abbel, D. Tordera, M. Sessolo, G. Gelinck and H. J. Bolink, *ACS Appl. Mater. Interfaces*, 2018, **10**, 41586–41591.
6 Z. Yang, Z. Mao, Z. Xie, Y. Zhang, S. Liu, J. Zhao, J. Xu, Z. Chi and M. P. Aldred, *Chem. Soc. Rev.*, 2017, **46**, 915–1016.
7 X. Yang, G. Zhou and W.-Y. Wong, *Chem. Soc. Rev.*, 2015, **44**, 8484–8575.
8 J. Tagare and S. Vaidyanathan, *J. Mater. Chem. C*, 2018, **6**, 10138–10173.

9 W. Wu, C. Z. Jiang and V. A. L. Roy, *Nanoscale*, 2016, **8**, 19421–19474.
10 X. He, Z. Zhao, L.-H. Xiong, P. F. Gao, C. Peng, R. S. Li, Y. Xiong, Z. Li, H. H.-Y. Sung, I. D. Williams, R. T. K. Kwok, J. W. Y. Lam, C. Z. Huang, N. Ma and B. Z. Tang, *J. Am. Chem. Soc.*, 2018, **140**, 6904–6911.
11 D. Xu, H. Zou and M. Liu, *J. Colloid Interface Sci.*, 2017, **508**, 248–253.
12 J. Li, X. Zhen, Y. Lyu, Y. Jiang, J. Huang and K. Pu, *ACS Nano*, 2018, **12**, 8520–8530.
13 J. Qi, C. Sun, D. Li, H. Zhang, W. Yu, A. Zebibula, J. W. Y. Lam, W. Xi, L. Zhu, F. Cai, P. Wei, C. Zhu, R. T. K. Kwok, L. L. Streich, R. Prevedel, J. Qian and B. Z. Tang, *ACS Nano*, 2018, **12**, 7936–7945.
14 V. Aruna, V. Aruna and Y. Gao., *ACS Appl. Bio Mater.*, 2018, **1**, 298–309.
15 K. Y. Zhang, Q. Yu, H. Wei, S. Liu and Q. Zhao, *Chem. Rev.*, 2018, **118**, 1770–1839.
16 S. M. A. Fateminia, Z. Mao, S. Xu, Z. Yang, Z. Chi and B. Liu, *Angew. Chem.*, 2017, **56**, 12160–12164.
17 J. F. d. S. Petruci, P. C. Hauser and A. A., *Sens. Actuators, B*, 2018, **268**, 392–397.
18 N. Kwon, Y. Hu and J. Yoon, *ACS Omega*, 2018, **3**, 13731–13751.
19 J. F. d. S. Petruci and A. A. Cardoso, *Anal. Chem.*, 2016, **88**, 11714–11719.
20 M. Lee, Y.-C. Jang, W. Den and P. Kuo, *Synthesis of Fluorogenic Chemosensors for Hg^{2+} Detection Using Naphthalimide Derivatives*, American Chemical Society, 2014, vol. 1184, pp. 49–69.
21 X. Zhou and S. Lee, *Chem. Rev.*, 2015, **15**, 7944–8000.
22 Z. Simić, Z. Stanić and M. Antonijevic, *J. Braz. Chem. Soc.*, 2010, **22**, 709–717.
23 N. Balázs and P. Sipos, *Carbohydr. Res.*, 2007, **342**, 124–130.
24 J. Fan, C. Lin, H. Li, P. Zhan, J. Wang, S. Cui, M. Hu, G. Cheng and X. Peng, *Dyes Pigm.*, 2013, **99**, 620–626.
25 S. Radunz, H. R. Tschiche, D. Moldenhauer and U. Resch-Genger, *Sens. Actuators, B*, 2017, **251**, 490–494.
26 K. Aggarwal and J. M. Khurana, *J. Photochem. Photobiol., A*, 2015, **307–308**, 1–18.
27 E. Faggi, J. Serra-Vinardell, M. D. Pandey, J. Casas and G. Fabriàs, *Sens. Actuators, B*, 2016, **234**, 633–640.
28 A. Thottiparambil, P. R. A. Kumar and L. Chakkumkumarath, *RSC Adv.*, 2014, **4**, 56063–56067.
29 M. Tian, X. Peng, J. Fan, J. Wang and S. Sun, *Dyes Pigm.*, 2012, **95**, 112–115.
30 D. Aigner, S. M. Borisov, F. J. O. Fernández, J. F. Fernández Sánchez, R. Saf and I. Klimant, *Talanta*, 2012, **99**, 194–201.
31 Y. Chen, C. Zhu, J. Cen, Y. Bai., W. He and Z. Guo, *Chem. Sci.*, 2015, **6**, 3187–3194.
32 P. Guo, L. Liu, Q. Shi, C. Yin and X. Shi, *J. Mol. Struct.*, 2017, **1130**, 150–155.
33 J. Fan, C. Lin, H. Li, P. Zhan, J. Wang, S. Cui, M. Hu, G. Cheng and X. Peng, *Dyes Pigm.*, 2013, **99**, 620–626.
34 R. Shi, L. Huang, X. Duan, G. Sun, G. Yin, R. Wang and J. Zhu, *Anal. Chim. Acta*, 2017, **988**, 66–73.
35 S. Munusamy and S. Kulathu Iyer, *Tetrahedron: Asymmetry*, 2016, **27**, 492–497.
36 S. Munusamy, V. P. Muralidharan and S. K. Iyer, *Sens. Actuators, B*, 2017, **250**, 244–249.
37 S. K. Munusamy, K. Thirumoorthy, V. Panyam Muralidharan, U. Balijapalli and S. Kulathu Iyer, *Sens. Actuators, B*, 2017, **244**, 175–181.
38 M. Venkatesan and S. Kulathu Iyer, *Sens. Actuators, B*, 2018, **267**, 373–380.
39 M. Venkatesan and K. I. Sathiyanarayanan, *Sens. Actuators, B*, 2018, **267**, 373–380.
40 V. P. Gupta, in *Principles and Applications of Quantum Chemistry*, ed. V. P. Gupta, Academic Press, Boston, 2016, pp. 155–194.
41 A. Charaf-Eddin, A. Planchat, B. Mennucci, C. Adamo and D. Jacquemin, *J. Chem. Theory Comput.*, 2013, **9**(6), 2749–2760.
42 A. D. Becke, *Phys. Rev. A: At., Mol., Opt. Phys.*, 1988, **38**, 3098–3100.
43 C. Lee, W. Yang and R. G. Parr, *Phys. Rev. B: Condens. Matter Mater. Phys.*, 1988, **37**, 785–789.
44 J. Tomasi, B. Mennucci and R. Cammi, *Chem. Rev.*, 2005, **105**, 2999–3093.
45 R. E. Stratmann, G. E. Scuseria and M. J. Frisch, *J. Chem. Phys.*, 1998, **109**, 8218–8224.
46 M. E. Casida, C. Jamorski, K. C. Casida and D. R. Salahub, *J. Chem. Phys.*, 1998, **108**, 4439–4449.
47 M. J. Frisch. G. W. Trucks. H. B. Schlegel. G. E. Scuseria. M. A. Robb, J. R. Cheeseman, *et al.*, *Gaussian 09*, Gaussian, Inc., Wallingford, CT, USA, 2009.
48 T. Keith and J. Millam, *GaussView, version 5.0.9*, Semichem Inc., Shawnee Mission, KS, USA, 2009.
49 K. S. Pawan, C. Navneet, K. Pawan, S. Chetan and R. A. Kamal, *Eur. J. Med. Chem.*, 2011, **46**, 1425.
50 S. Xia and H. Liu, *Bioconjugate Chem.*, 2018, **29**, 1406–1418.
51 H. Liu, R. L. Luck, H.-M. Lee and J. Wang, *J. Mater. Chem. B*, 2019, **7**, 198–209.
52 X. Song and X. Liu, *Anal. Chem.*, 2017, **89**, 7038–7045.